Advanced Functional Materials

ADVANCED FUNCTIONAL MATERIALS
www.afm-journal.de

RESEARCH ARTICLE OPEN ACCESS

Boosting Conversion Efficiency in Zn_3P_2/InP Solar Cells Via Nanoscale Junction Engineering

Raphael Lemerle[1] | Valerio Piazza[1] | Andrea Filippo[1] | Melanie Micali[2] | Luna Warzawa[2] | Thomas Hagger[1] | Kamil Wodzislawski[1] | Julien Hurni[3] | Valentin Biselli[1] | Ioannis Kalogerakis[4] | Konstantinos Rogdakis[4] | George Viskadouros[4] | Emmanuel Kymakis[4] | Esther Alarcon-Llado[2,5] | Anna Fontcuberta i Morral[1,6]

[1]Laboratory of Semiconductor Materials, Institute of Materials, School of Engineering, Lausanne, Switzerland | [2]Center for Nanophotonics, LMPV, NWO-Institute AMOLF, Amsterdam, The Netherlands | [3]Laboratory of Photovoltaics and Thin Film Electronics (PV-Lab), Institute of Electrical and Microengineering, Neuchatel, Switzerland | [4]Department of Electrical and Computer Engineering, Hellenic Mediterranean University, Heraklion, Greece | [5]Van't Hoff Institute for Molecular Sciences (HIMS), University of Amsterdam, Amsterdam, The Netherlands | [6]Institute of Physics, School of Basic Sciences, Lausanne, Switzerland

Correspondence: Raphael Lemerle (mdehghan@aut.ac.ir) | Anna Fontcuberta i Morral (mdehghan@aut.ac.ir)

Received: 17 April 2026 | **Revised:** 21 July 2026 | **Accepted:** 4 August 2026

Keywords: electron diffusion length | indium phosphide | photovoltaics | selective area epitaxy | zinc phosphide

ABSTRACT

Zinc phosphide (Zn_3P_2) shows great promise for next-generation photovoltaics made of earth-abundant elements. To date, the poor crystal quality is limiting conversion efficiency to 4.4% for heterojunction and to 6% for Schottky junction solar cell. This work presents the fabrication and characterization of Zn_3P_2/InP solar cells with a new record efficiency of 8%. The material quality is significantly improved by using selective area epitaxy (SAE) in conjunction with a post-growth annealing. The combination of current–voltage (J–V) measurements and electron beam induced current (EBIC) mapping, alongside with optical and electrical simulations, outline the impact of the SAE pattern dimensions on the device performances. A decrease in the opening area fraction is associated with an increase in the V_{OC} and a decrease in the J_{SC}. Our results suggest that the degradation of the V_{OC} for large openings is predominantly attributable to the presence of misfit dislocations at the heterojunction interface. On the other hand, the reduced J_{SC} for small openings is associated with a smaller electron diffusion length, which is attributed to the current crowding effect. Finally, the device's stability under outdoor testing over a year is demonstrated.

1 | Introduction

In the context of the energy transition, advancing semiconductor materials that enhance the sustainability of photovoltaic devices is essential. Zinc phosphide (Zn_3P_2) stands out as a good candidate for next-generation thin-film PV: composed of earth-abundant elements, it combines an ideal direct bandgap (1.5 eV) with a very high visible-range absorption coefficient ($\geq 10^4$ cm^{-1}), making it intrinsically well suited for efficient, low-material-cost solar absorbers [1–3]. In the last decades, the record power conversion efficiency (PCE) for a device based on Zn_3P_2 has been limited to 6% [4]. This relatively poor performance may be attributed to several factors. First, the production of Zn_3P_2 with adequate crystal quality poses a considerable challenge due to its large unit cell and thermal expansion coefficient [5]. Epitaxial growth often leads to the formation of a large number of structural defects in the film, which limits the electron/hole diffusion length [6]. Zn_3P_2 is sensitive to ambient moisture, which degrades its properties over time; recent studies have shown that effective surface protection is essential to preserve its stability

[7]. Furthermore, controlling doping in Zn_3P_2 is challenging: low formation energies of acceptor defects (notably zinc vacancies) render the material intrinsically p-type, complicating n-type doping and device engineering [2, 8–10]. Attempts to obtain high mobility n-type Zn_3P_2 by external doping have been unsuccessful due to the self-compensation effect. Katsube et al. demonstrated n-type Zn_3P_2 with a carrier concentration of up to 10^{13} cm^{-3} by doping it with In, but the resulting resistivity was too high for a proper device operation [11]. Because reliable homojunctions in Zn_3P_2 remain impractical, a Schottky-junction strategy was preferred. This approach underpinned the highest-performance Zn_3P_2 solar cell to date, employing a Mg/Zn_3P_2 Schottky contact [4]. Alternatively, heterojunctions offer a promising route: recent studies showed that pairing high-quality Zn_3P_2 with an optimal n-type semiconductor can yield substantially higher efficiencies [12, 13]. Several n-type emitters have been explored and some of the fabricated heterojunction devices have demonstrated superior open-circuit voltage (V_{OC}) or short-circuit current (J_{SC}) in comparison to the Mg/Zn_3P_2 solar cell. For example, a Zn_3P_2/ZnSe solar cell demonstrated a record V_{OC} of 810 mV, but for a PCE of only 0.8% [13]. On the other side, a record J_{SC} of 18.4 mA/cm^2 was obtained for a Zn_3P_2/ITO solar cell, with a PCE of 2.1% [14]. In both cases, the low efficiency can be partially explained by the poor crystal quality of Zn_3P_2.

We recently started to investigate InP to function as both an n-type emitter and a substrate for the growth of Zn_3P_2. At first glance, InP does not appear to be an optimal n-type emitter, mostly because of the substantial conduction band offset between the two materials (approximately 0.8 eV [13, 15]) that constrains the maximum attainable V_{OC}. Nevertheless, it is considered one of the most optimal substrates to grow Zn_3P_2 with high crystal quality. Despite the substantial disparity in thermal expansion coefficients between the two materials ($1.4 \cdot 10^{-5}$ K^{-1} for Zn_3P_2 and $4.6 \cdot 10^{-6}$ K^{-1} for InP at room temperature [5, 16]), the lattice mismatch between the phosphorous sub-lattice of Zn_3P_2 (a = 5.7 Å) and the phosphorous lattice of InP (a = 5.9 Å) is relatively small (2.4%) [17]. Monocrystalline Zn_3P_2 has been successfully grown on InP and hole mobilities up to 125 cm^{-2}/(Vs) were reported [17, 18]. In a recent study, we manufactured a Zn_3P_2/InP solar cell that demonstrated a record efficiency of 4.4% for Zn_3P_2-based heterojunction solar cells [19]. Our measurements indicated that only a negligible amount of the light was converted into the Zn_3P_2 film; most of the current was generated in the InP substrate. Several factors explain the negligible Zn_3P_2 contribution. Band-diagram simulations indicate that the ITO top contact does not effectively drive electrons toward the depletion region at the Zn_3P_2/InP interface, preventing efficient carrier collection from the absorber [19]. Furthermore, structural defects in the film may strongly limit the diffusion length of minority carriers [19, 20]. Finally, the thickness of the active layer grown on InP is restricted to less than 1 μm, above which cracks start to form [18], which restricts the portion of light absorption. To improve the crystal quality, we have explored the possibility of growing the film by selective area epitaxy (SAE), using a SiO_2 mask patterned with nanoholes [21]. The growth initiate by the formation of pyramidal nanostructures which subsequently coalesce at a subsequent stage. Scanning transmission electron microscopy (STEM) measurements revealed full strain relaxation without the formation of a substantial amount of dislocations. A comprehensive investigation into the electrical properties of the films revealed hole mobilities of up to 560 cm^2/(Vs), a record for Zn_3P_2. This finding demonstrates the effective carrier transport in the film [22].

In this work, we demonstrate a Zn_3P_2/InP solar cell with a new record efficiency of 8.0%. We investigate the properties of the solar cells fabricated from Zn_3P_2 thin films grown by SAE on InP substrates. The combination of current–voltage (J–V), external quantum efficiency (EQE), and electron beam induced current (EBIC) measurements with coupled optical and electrical simulations provide a comprehensive understanding of the conversion mechanisms in the device. The emphasis is placed on understanding the effect of the mask pattern on the device performances. The impact of the growth conditions and post-growth annealing is also briefly investigated. Finally, the long-term outdoor PCE performance and lifetime stability of the devices is demonstrated through J–V and maximum power point tracking (MPPT) measurements acquired over the course of one year in the Hellenic Mediterranean University (HMU) Solar Farm.

2 | Results and Discussion

2.1 | Effect of Pattern and Growth Conditions on SC Performances

The solar cells devices are fabricated from Zn_3P_2 thin films grown on undoped InP (intrinsically n-type) by SAE. The fabrication procedure for the devices is illustrated in Figure 1 and is described in more detail in the experimental section.

We start with a comprehensive study of the effect of the pattern geometry and the growth conditions on the solar cell performances. Figure 2 presents the results of J–V measurements conducted on various devices. Figure 2a highlights the effect of the growth temperature and the area fraction (AF) on the solar cell performance. The AF is calculated from the hole radius R and the pitch P using the following expression:

$$AF = \left(\frac{\pi R^2}{P^2}\right) \cdot 100 \quad (1)$$

One can observe that the reduction of the area fraction leads to a decrease of the short-circuit current (J_{SC}) and an increase of the open-circuit voltage (V_{OC}). This trend is consistent with our recent simulation study, which explores via numerical simulation the expected impact of the area fraction on PV performance [23]. The enhancement of the V_{OC} is attributed to the reduction in surface recombination velocity at the Zn_3P_2/InP interface, a phenomenon that arises from the reduced contact area. On the other hand, the J_{SC} degradation for smaller AF is explained by an increased series resistance because of narrow openings and a decreased optical absorption in Zn_3P_2. The latter is attributable to two factors: reduced back-reflectance resulting from the SiO_2 interface and smaller volume of Zn_3P_2 in the region of the mask. Although this region is only 25 nm thick, reducing the absorber volume can have a significant impact due to its proximity to the depletion region. Another lesson from this figure is that, for all the different AFs, the highest growth temperature (300°C) leads to the best performance in both V_{OC}

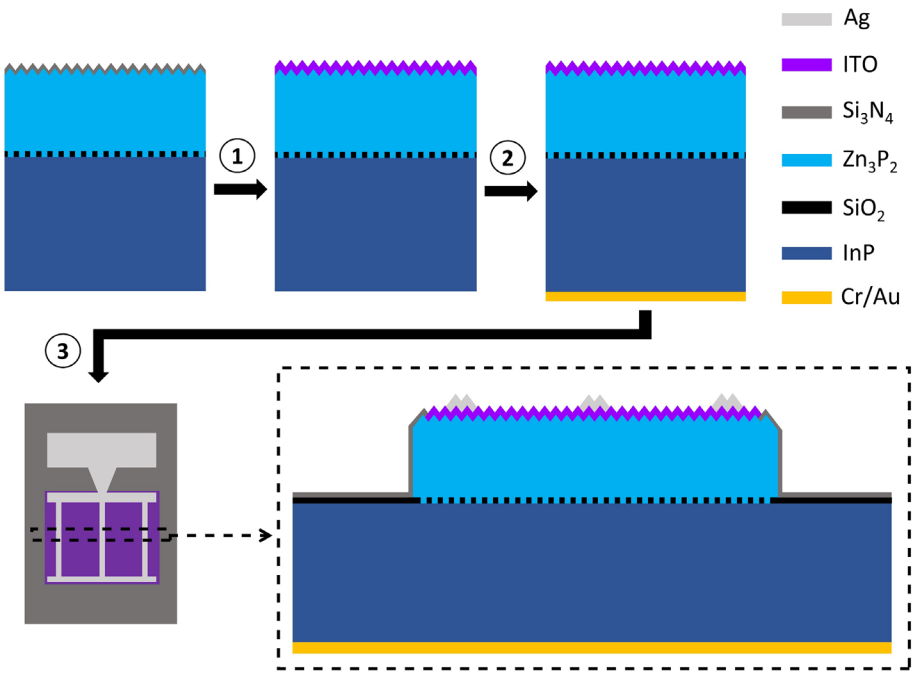

FIGURE 1 | Schematic representation of the fabrication of the SAE Zn_3P_2/InP solar cell. The Si_3N_4 protective layer on top of Zn_3P_2 is removed by HF, followed by the deposition of ITO at the top (step 1), Au at the back (step 2) and finally deposition of a Ag grid on top of ITO (step 3).

and J_{SC}. This finding aligns with our previous study, in which we observed an increase in photoluminescence (PL) emission of Zn_3P_2 grown at higher temperatures [22]. An increased PL emission is indicative of reduced non-radiative recombination, which would improve both the V_{OC} and the J_{SC}. However, the underlying mechanisms responsible for the observed correlation between growth temperature and PL emission remains unclear and would require further investigation.

Using the same growth conditions, thin films grown from different AFs have different thickness, because the growth rate is affected by the pattern [22]. Therefore, a set of samples was generated with varying growth durations to decouple the effects of pattern and thickness on device performance. All the samples were grown at 290°C. The evolution of the PCE, as reported in the Figure S1, demonstrates an enhancement in performance with decreasing hole size, but no discernible trend is observed with pitch. Figure 2b shows the evolution of the V_{OC} with thickness for different patterns. One can see that the V_{OC} remains approximately constant with thickness, which is consistent with the anticipated behavior of a thin film exhibiting good crystal quality. Again, the trend of the mean V_{OC} with respect to the AF is consistent with the simulations. Nevertheless, the improvement of the V_{OC} is more pronounced than anticipated for decreasing hole size. Within the range of AF considered (from 28.3% to 2.5%), the V_{OC} gain determined experimentally is equal to 0.33 V, which is significantly higher than the 0.06 V gain predicted by simulations. Our recent study revealed the formation of misfit dislocations at the Zn_3P_2/InP interface only for large hole sizes [22]. These defects could have a significant impact on the V_{OC} by increasing the amount of recombination at the interface.

Figure 2c shows the evolution of the J_{SC} with the thickness for different patterns. We can see that increasing the thickness results in a reduction in J_{SC}. This effect can be elucidated through the use of optical simulations. Figure 2d compares the simulated photocurrent (J_{ph}) in each absorbing layer (assuming no electrical losses) with the experimental J_{SC} for samples grown from a 120/400 pattern. First, it is evident that the experimental J_{SC} is much lower than the total simulated J_{ph}, indicating substantial electrical losses. Then, we can see that the total simulated J_{ph} slightly diminishes with thickness, which is attributed to the evolution of the surface morphology. It has been established that the top surface becomes flatter with increasing thickness [22]. This results in an increase in reflectance due to a reduced light trapping effect engendered by the pyramidal texturing [24]. From the simulated reflectance spectra shown in the see Figure S2, we can compute the average reflectance for each sample. We observe that the mean reflectance exhibits a slight increase with thickness, going from 10.5% to 12.9%.

Nevertheless, reduced light trapping leading to a slight decline in J_{PH} (3.7% loss), cannot fully explain the more pronounced decrease in experimental J_{SC} (29.8% loss). To facilitate a more profound comprehension, one can look at the different simulated contributions coming from Zn_3P_2 and InP. The photogenerated current in Zn_3P_2 increases with a larger volume of material due to greater light absorption. On the other hand, the photogenerated current in InP decreases with a larger volume of Zn_3P_2, because the thicker Zn_3P_2 film hinders the incoming light. In the solar cell study by Paul et al., it was established that the majority of the collected current originated from the InP [19]. This hypothesis can be verified by comparing the external quantum efficiency (EQE) spectrum with the simulated absorption spectra of the two absorbers. This experiment was conducted on a device with a 1200 nm thick layer of Zn_3P_2, the result of which is shown in the Figure S3. A thorough examination of the spectra corroborates the hypothesis that the majority of the photocurrent generated

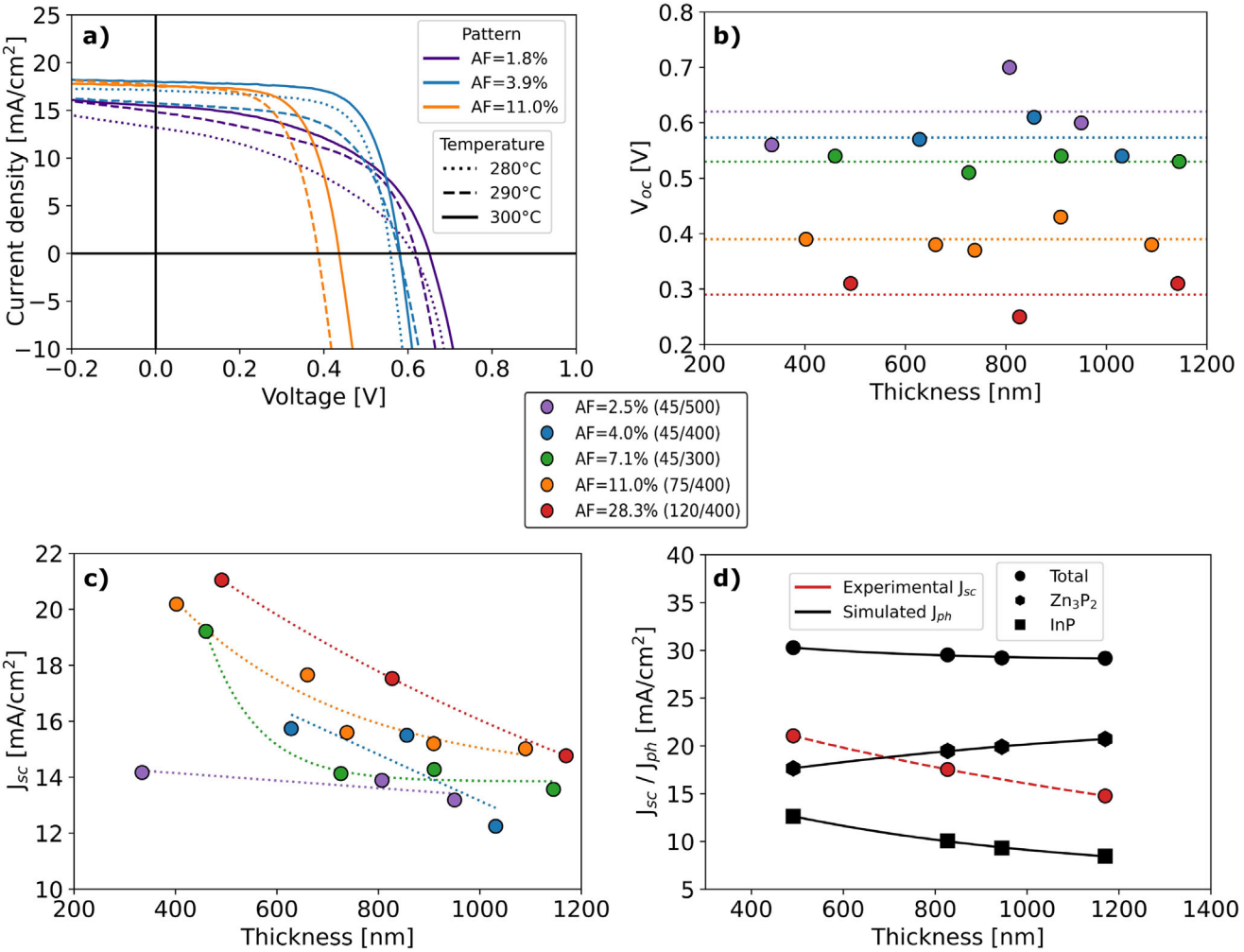

FIGURE 2 | Performances of the fabricated solar cell devices. All J–V measurements are performed using the 1st setup. (a) Comparatives J–V curves of devices based on Zn_3P_2 thin films grown with various pattern dimensions at different temperatures. Evolution of the (b) V_{OC} and the (c) J_{SC} with thickness for different AFs for samples grown at 290°C. (d) Simulated J_{PH} generated in the device (in black) compared with the experimental J_{SC} (in red) for samples grown from a 120/400 pattern at 290°C.

within the solar cell is attributable to the InP layer. Consequently, we believe that the degradation of the J_{SC} with the thickness is predominantly attributable to reduced light absorption in the InP.

Finally, by subtracting the InP photocurrent from the J_{SC}, we can compute the lower bound estimation of the Zn_3P_2 contribution to the J_{SC}, based on the assumption that 100% of the photogenerated current in InP is collected. We find that the Zn_3P_2 contribution decreases with the thickness going from 8.42 mA/cm^2 (40% of J_{SC}) to 6.31 mA/cm^2 (42% of J_{SC}). This could be due to carrier generation occurring farther away from the depletion region or to degradation of the carrier transport with thickness.

2.2 | Determination of Minority Carrier Diffusion Length by EBIC

The enhancement in short-circuit current for larger area fraction, exhibited in Figure 2a,c, is consistent with the outcomes of our recent simulation study [23]. Still, the trend observed experimentally appears more pronounced than expected. Simulations estimate a difference in J_{sc} around 1.2 mA/cm^2 between the largest AF (28.3%) and the smallest AF (2.5%). Devices with thickness around 800 nm instead show a variation of J_{sc} around 3.6 mA/cm^2 (see Figure 2c), suggesting that the overall current collection may be defined by the interplay of multiple effects at once.

Electron beam-induced current mapping (EBIC) is a technique that enables the observation of localized mechanisms governing carrier transport with nanometric resolution. By exciting e^-/h^+ pairs with a scanning electron beam, EBIC allows to identify internal electric field and visualize current flowing through rectifying elements [25–28]. We therefore performed EBIC measurements by contacting top and bottom contact in situ with micromanipulators as done in previous works [29]. Secondary electrons are detected simultaneously enabling to record SEM/EBIC images at once. Results are shown in Figure 3 (data analysis reported in Figures S5 and S6). The measurements were performed by scanning the device cross-sections exposed to the electron beam after cleaving. Although it requires the formation of a new free surface, thus worsening carrier transport,

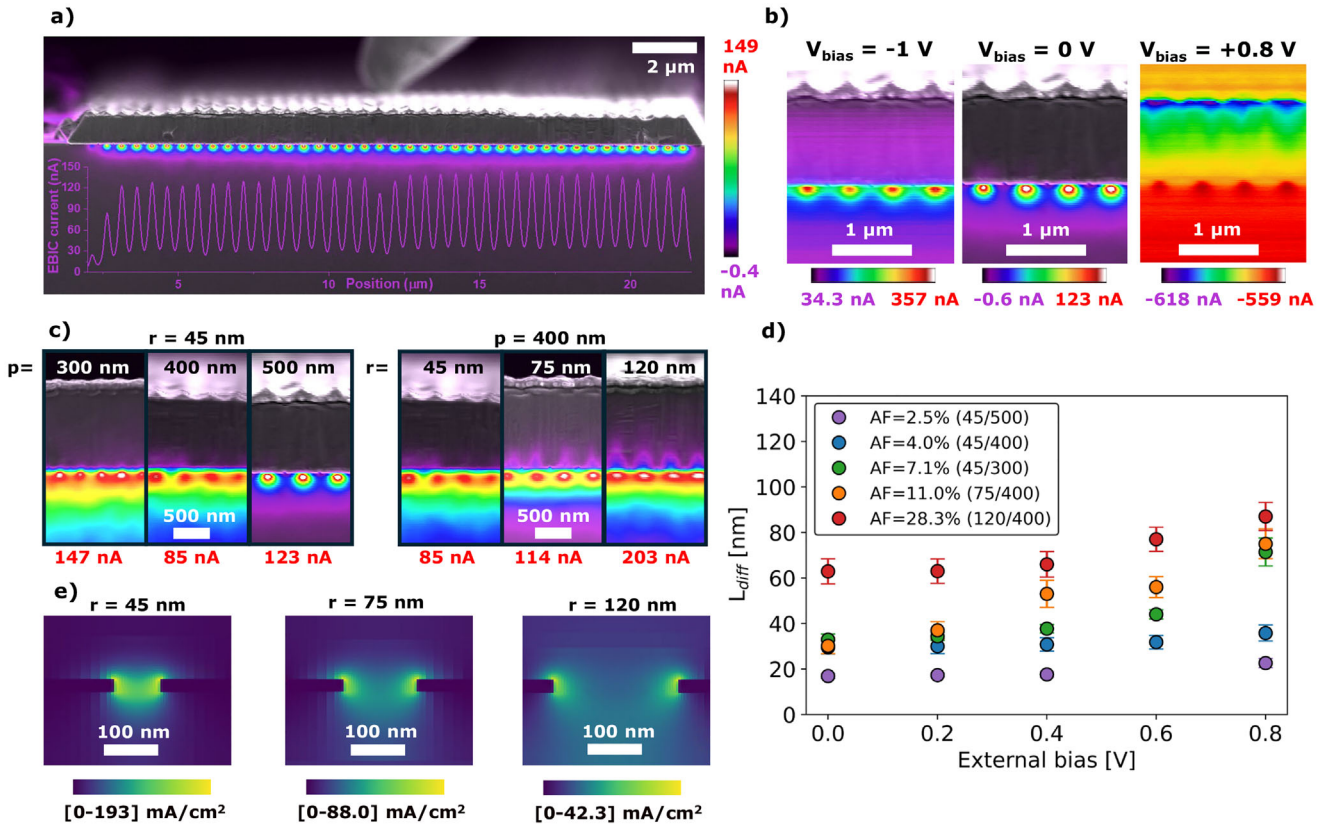

FIGURE 3 | Cross-sectional EBIC analysis of the Zn_3P_2/InP heterojunction. (a) Overlaid SEM/EBIC image of a full 45/500 array displaying the current generated locally at the heterointerface. The plot (in purple) highlights homogeneous current collection throughout the array. (b) High magnification SEM/EBIC maps of the same region as a function of external bias. (c) High magnification SEM/EBIC maps of different arrays varying pitch (left) and opening size (right). (d) Electron diffusion length in Zn_3P_2 as a function of the external bias for arrays with different hole size and pitch. (e) Finite element simulation of electron current density through a pinhole. All the EBIC maps are displayed in false color. Each panel shows the corresponding current values.

the cross-sectional configuration is needed to visualize carrier transport across the heterojunction [30, 31].

Figure 3a shows a cross-section SEM image of a device fabricated from a 45/500 pattern, combined with the EBIC signal. As expected, the micrograph shows a peak in EBIC signal at the opening position, where the p-Zn_3P_2/n-InP heterojunction is located. Moreover, the signal is modulated consistently with the 500 nm pitch and the extracted signal is extremely homogeneous across the array. The current profile (in purple) across the width of the array highlights the superior reproducibility of the heterointerface achieved by selective area growth. It is also important to note that the EBIC current is mostly collected from the InP substrate, consistently with the EQE measurements, supporting the hypothesis that most of the electrical current originates from the substrate.

Bias-dependent EBIC measurements (Figure 3b) allows to artificially widen the space charge region while increasing the signal to noise ratio thus offering another path to outline the contribution from Zn_3P_2 [32, 33]. Under forward bias, (V_{bias} = +0.8 V), EBIC shows an increase of dark current (noise of the map) and a weakening of the built-in field (intensity decrease of the localized signal at the heterointerface). Both effects are expected in a p-n junction. Furthermore, the arising of a strong signal with opposite polarity at the ITO/semiconductor interface confirms the band bending reported by Paul et al. [19]. Under reverse bias (V_{bias} = -1.0 V) instead, the measurements reveal a significant increase of the collected current but no visible widening of the space charge region into the Zn_3P_2 layer. Additional measurements on similar samples (reported in Figure S6) suggest an extension of the space charge region well below the size of the interaction volume thus preventing its visualization. This represents a major limitation for the device performance, which needs to be tackled in future work.

Despite the apparent absence of charge drift in Zn_3P_2, minority carriers photogenerated in this layer can contribute to the short-circuit current by diffusing into the depletion region. We therefore turned into a comparison of induced current collected as a function of hole diameter and pitch. SEM/EBIC micrographs are reported in Figure 3c. Interestingly, the EBIC signal in the InP substrate appears less localized by decreasing pitch or increasing hole size. This is a visualization artifact arising from the convolution of the interaction volume (estimated around 80 nm by Casino simulation as reported in Figure S6) and the lateral extension of the space charge region plus the contribution from the lateral diffusion of carriers in InP (estimated around 400 nm). The variation in EBIC diffusion tails in the Zn_3P_2 layers instead is a direct assessment of the capability to extract carriers generated in the top part. The SEM/EBIC maps in Figure 3c indicate that

electron diffusion mildly decreases with pitch and significantly increases with hole size. The corresponding minority carrier diffusion length values, shown in Figure 3d, are extracted by applying a simple 1D Poisson equation model [34, 35] (reported in Figure S6). As customary, the diffusion length values are extracted by varying the external bias. The extracted diffusion values are mostly voltage insensitive with minor deviations from the expected constant trend at larger bias. The estimated values obtained by this analysis reveal an increase of the electron diffusion length in zinc phosphide with increasing AF, with average values going from 19 to 71 nm. The result is counterintuitive to some extent, as one would expect an increased defect density with increasing hole size which would limit carrier diffusion. Nevertheless, it is consistent with the variation of the short-circuit current density reported in Figure 2e. EBIC measurements on devices with different Zn_3P_2 thickness (reported in Figure S7) do not reveal any significant impact on diffusion length, suggesting that transport mechanisms in this set of samples is not limited by the crystal quality.

One can also note that the diffusion length values extracted here are substantially lower than those reported in the literature for Zn_3P_2. Kimbal et al. reported a minority carrier diffusion length of at least 7 μm, as determined by time-resolved photoluminescence (TRPL) measurements [36], which is representative of carrier diffusion in the bulk. Our experimental setup instead requires creating free surface to scan through the junction, thus it is expected to retrieve lower diffusion length values due to surface recombination. The low acceleration voltage of the primary beam enabling the investigation of individual opening enhances even further the impact of surface recombination. Nonetheless, surface recombination cannot account for the evolution of minority carrier diffusion length with the opening geometry. Furthermore, the photocurrent collection in Zn_3P_2 is comparatively small for all devices, with a maximum of 8.4 mA/cm^2 for large area fraction, thereby supporting the hypothesis of a low electron diffusion length. This may be due to recombination through intrinsic trap states within the bulk such as Zn interstitials [37] or to the Zn_3P_2/InP interface.

To better understand how hole size affects diffusion length, three-dimensional simulations of electron transport through a pinhole with radius ranging from 45 to 120 nm were conducted using Nextnano (Figure 3e). The results of the simulation indicate the presence of a significant current crowding effect around the sides of the openings. This effect is particularly pronounced for small apertures, as it extends to the full extent of the opening. A significant accumulation of electrons may result in more recombination [38], thereby elucidating the observed decrease in diffusion length. An other possible explanation for the low diffusion length may be attributed to the carrier concentration in Zn_3P_2. In our recent study, we observed an increase in carrier concentration with decreasing thickness, which may be due to the presence of a p^+-doped layer in proximity to the Zn_3P_2/InP interface [22]. This would account for both the small depletion region and the reduced diffusion length. Finally, at a forward bias of +0.8 V, a signal with an opposite polarity compared to the pn junction is observed at the Zn_3P_2/ITO interface (reported in Figure S8). The weak rectifying nature of this contact was already reported in a previous publication [19]. From this signal, an electron diffusion length of 250 nm can be extracted, which is significantly higher than the reported values for the diffusion tail of the Zn_3P_2/InP interface. This observation lends support to the hypothesis that, in this device, the principal factor limiting diffusion is current crowding at the Zn_3P_2/InP interface, rather than crystal quality.

2.3 | Annealing Study and Record Solar Cell

We also explored the effect of thermal annealing on the device performances. For this experiment, we use a set of samples grown at 300°C with various AFs (pitch of 400 nm and hole size ranging from 30 nm to 75 nm). The annealing is performed at 300°C for 30 min in N_2 atmosphere after the device fabrication. Figure 4a–d shows the evolution of each performance parameter with the AF and how this evolution is affected by the thermal annealing. We observe a strong decrease of V_{OC} when increasing AF but after annealing, the degradation of the V_{OC} with larger AF is much less dramatic. The V_{OC} improvement due to annealing is substantial for large hole size and minor for small hole size. This supports the idea that the misfit dislocations present at the Zn_3P_2/InP interface, for large hole size only, may have a significant impact on the V_{OC}. Furthermore, the results suggest that a thermal annealing at 300°C could be a viable method for reducing the number of these defects. Misfit dislocations reduction or rearrangement with annealing has already been reported in literature [39, 40]. This hypothesis would require a deeper investigation which is outside the scope of this study.

Looking at Figure 4b, we don't see clear trend for the evolution of J_{SC} with AF because the increase in AF is concomitant with an augmentation in thickness. In addition, a marginal enhancement in the J_{SC} can be observed following annealing, with the exception of the smaller area fraction, where a substantial improvement in the J_{SC} is evident. The minor improvement in J_{SC} could be due to a reduction of absorption losses in the ITO. We know that annealing at temperature higher than 180°C results in the crystallization of amorphous ITO [41, 42]. This is often associated with an increase of the transmittance in the visible light, which could explain the small improvement of the J_{SC} [42, 43]. Furthermore, the augmentation in shunt resistance (going from 215 Ω.cm^2 to 585 Ω.cm^2) measured for the smaller AF could explain the major improvement of both J_{SC} and FF for this specific device. However, as shown in Figure 4c, the FF degrades with annealing for the other devices, which is mostly due to an increase of the series resistance (going from 2.84 Ω.cm^2 to 7.14 Ω.cm^2 for the AF = 3.9% sample). We believe that the observed increase in series resistance is associated with the metal contacts. In the Figure S9, comparative J–V curves are presented for two devices fabricated from the same thin film (grown from a AF = 3.9% pattern). One of the devices underwent thermal annealing after the ITO deposition. It can be seen that all the parameters, including the FF, are improved with annealing. This corroborates the hypothesis that higher resistance is present in the metals or at one of the metal interfaces. There are several examples in literature where an increase of the contact resistance for ITO/Ag contacts with annealing is observed [43, 44]. One of the main explanation is the diffusion of Ag, even at temperatures below 300°C, into the ITO and also sometimes into the absorber [44]. Therefore, we recommend to perform the annealing prior to the deposition of metal contacts.

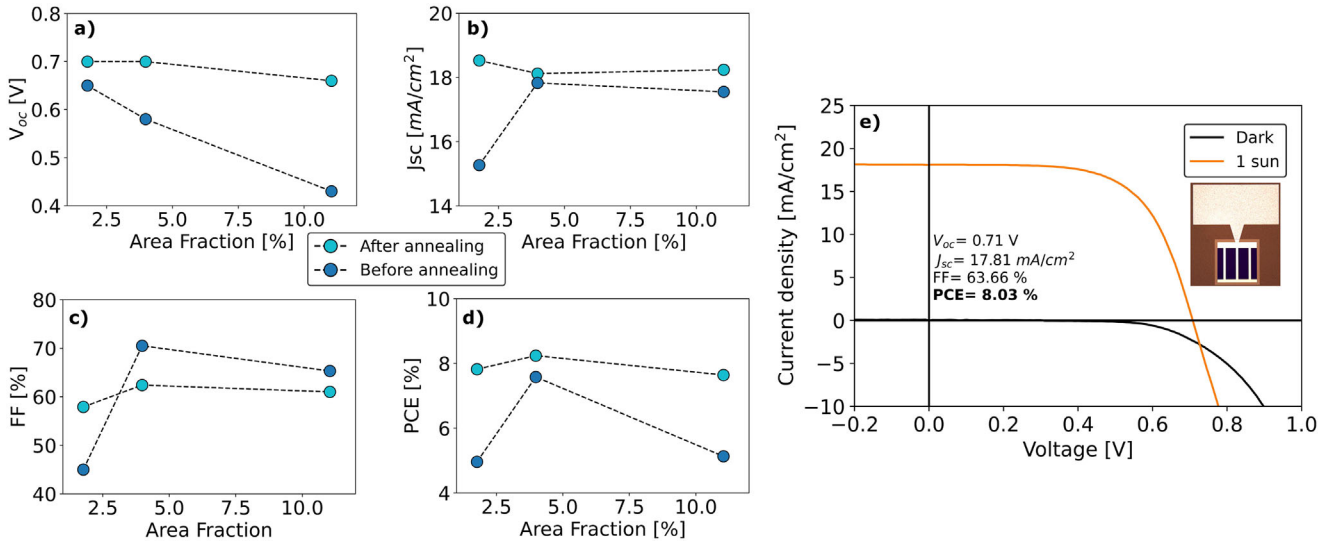

FIGURE 4 | Evolution with AF of the (a) V_{OC}, (b) J_{SC}, (c) FF and (d) PCE for samples grown at 300°C before and after annealing. (e) J–V curves of the champion device obtained in dark (denoted by black line) and under 1-sun illumination (denoted by orange line), the inset shows the measured device that had an active area of 0.0032 cm^2.

Finally, Figure 4d shows that for all samples, the annealing improves the PCE. The best efficiency of 8.2% is obtained for the device fabricated from a 45/400 pattern (AF = 4%). The optimal area fraction estimated by simulations is around 8%, but this does not consider the difference in Zn_3P_2 thickness for our samples [23]. The champion device was also measured using an other measurement setup under standard test conditions (STC). The differences between the two setups are explained in more details in the experimental section. The measurement from the STC setup resulted in an efficiency of 8.0%, as illustrated in Figure 4e. Only this result should be considered relevant to define the record conversion efficiency. The open-circuit voltage of V_{OC} = 0.71 V is improved by 44% compared to the Zn_3P_2/Mg solar cell and by 34% compared to the previous Zn_3P_2/InP solar cell [4, 19]. The short-circuit current of J_{sc} = 17.81 mA/cm^2 is improved by 19% compared to the Zn_3P_2/Mg solar cell and by 30% compared to the previous Zn_3P_2/InP solar cell. Furthermore, the shunt resistance R_{Shunt} = 8.04 kΩ.cm^2 is one order of magnitude higher compared to the previous Zn_3P_2/InP solar cell, which highlights a significant reduction of the leakage current. However, the series resistance of 7.48 Ω.cm^2 is roughly 3 times bigger. As previously discussed, this phenomenon may be attributable to the annealing of the metal contacts. The series resistance before annealing (2.84 Ω.cm^2) is very close to the previous Zn_3P_2/InP solar cell (2.56 Ω.cm^2). Similar to Paul et al. we observe a crossover of the 1 sun curve with the dark curve [19]. We also performed EQE measurements for this device. The resulting spectrum is compared with the simulated absorption spectra in the Figure S4, and confirms that the majority of the photocurrent generated within the solar cell is attributable to the InP layer. Furthermore, the simulations allow for the calculation of the maximum photocurrent generated in both layers: 17.76 mA/cm^2 for Zn_3P_2 and 12.19 mA/cm^2 for InP. Under the assumption that 100% of the photogenerated current in InP is collected, we can estimate the lower bound value of the Zn_3P_2 contribution to the photocurrent to be equal to 5.62 mA/cm^2 (31% of J_{SC}). This is to compare with the Zn_3P_2 contribution for the previous Zn_3P_2/InP solar cell, estimated around 3.3 mA/cm^2 [19]. Therefore, it is evident that the extraction of the charge carrier in the Zn_3P_2 layer has been enhanced with this new device.

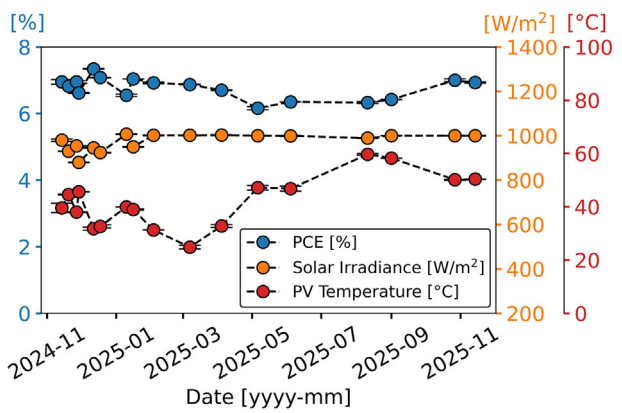

FIGURE 5 | Outdoor measurement of a device fabricated from a 45/400 pattern. Evolution of the PCE, Solar irradiance and PV temperature over a full year.

2.4 | Long Term Stability Measurements

We finally assess the long-term stability of a solar cell exposed to outdoor conditions in Heraklion, Greece, for a duration of one year. The device used for outdoor measurements was fabricated from a Zn_3P_2 thin film grown from a 45/400 pattern at 290°C, with a V/II ratio of 1.3 for 6 h. J–V measurements were performed at least once per week in conjunction with the collection of meteorological data. The results of this study are shown in Figure 5. We can observe a stable PCE over the year, with a slight seasonality effect observed mainly during summer period. The evolution of the PCE demonstrates a significant correlation with the temperature of the PV cell. The increase in temperature toward the summer results in a decline in PCE, while a drop in temperature during winter leads to a an increase in PCE, reaching

a level comparable to that recorded one year prior. The decline in efficiency with increasing temperature is a phenomenon that has been widely documented for major PV technologies [45]. Determining the effect of the average irradiance on the PCE is difficult due to the small annual fluctuations. A more advanced study will be conducted to gain a deeper understanding of how specific meteorological conditions influence performance. To conclude, we demonstrate that our device exhibits remarkable stability under outdoor conditions with relatively high irradiance, temperature, and humidity. Previous studies have shown that Zn_3P_2 is sensitive to exposure in air and water [7, 46]. Therefore, we deduce that the ITO acts as an efficient protective layer for a solar cell based on Zn_3P_2.

3 | Conclusion

In conclusion, this study demonstrates the efficacy of selective area epitaxy in enhancing the performance of a solar cell device. First, the improved crystal quality of the Zn_3P_2 absorber is reflected in the higher open-circuit voltage and short-circuit current generated in the Zn_3P_2, compared to the previous Zn_3P_2/InP device. Furthermore, the incorporation of a nano-patterned SiO_2 layer between Zn_3P_2 and InP helps boosting the open-circuit voltage even further through a reduction in interface recombination. We found that the dimensions of the pattern have a significant impact on the performances: a smaller area fraction increases V_{OC} but decreases J_{SC}. The low V_{OC} for large openings is attributed to the presence of misfit dislocations at the Zn_3P_2/InP interface. We show that post-fabrication annealing at a moderate temperature of 300°C improves the performances of the device, especially for large openings. Furthermore, the combination of EBIC measurements with simulations reveals that the degradation of the J_{SC} for smaller openings is due to a reduction in electron diffusion length caused by current crowding. Our champion device was fabricated from a sample with a relatively small openings size (45/400), with post-growth annealing. We believe that the most effective approach to outperform our current record is to select a sufficiently large opening size and optimize the annealing conditions. Additionally, to overcome the limitation on electron diffusion length resulting from the reduced contact area at the Zn_3P_2/InP interface, the device architecture could be inverted by employing an p-type substrate and depositing an alternative n-type emitter on top of the Zn_3P_2 film. The use of more earth-abundant substrates, such as silicon or glass, should be explored as a means of eliminating the costly InP from the stack. Finally, we demonstrate the long-term stability of our technology by monitoring a stable PCE over a full year exposed outdoor.

4 | Experimental Section

4.1 | Material Growth

The substrate chosen for the growth is undoped InP (100), which is intrinsically n-type with a carrier concentration as low as 10^{15} cm^{-3}. The SAE pattern is fabricated using e-beam lithography, and Zn_3P_2 is grown using molecular beam epitaxy (MBE). The pattern fabrication and the growth procedure are both described in details in our recent study [22]. Two set of patterns are prepared. The first one consists of various 800 μm × 800 μm square arrays of nanoholes, which are intended for the subsequent fabrication of solar cells. The second one consists of various 20 μm × 200 μm strip arrays of nanoholes, which are intended for the subsequent fabrication of EBIC devices. Each array has a specific hole radius (ranging from 30 to 120 nm) and pitch (ranging from 300 to 500 nm). We explore samples grown with different V/II ratio, temperature and duration. All samples are covered by 20 nm of Si_3N_4 deposited by plasma-enhanced chemical vapor deposition (PECVD) to protect the film against oxidation [7].

4.2 | Device Fabrication

A first lithography step is performed to remove the protective Si_3N_4 layer on top of the Zn_3P_2 square and deposit a layer of ITO (step 1). The Si_3N_4 is etched by dipping the sample in 1% HF for 1 min 15 s. After an Ar milling step of 20 s to remove any native oxide, a 80 nm layer of ITO (In_2O_3:SnO = 90%:10%) is deposited by sputtering. Then, a 150 nm layer of Au is deposited by sputtering at the back of the InP substrate (step 2). Prior to the deposition, 60 s of Ar milling is performed to remove the InP native oxide, and 5 nm of Cr is deposited to ensure good adhesion of the Au. Finally, a second lithography step is performed to deposit the Ag grid by sputtering, with a nominal thickness of 150 nm (step 3). The Ag grid is connected to a pad sitting on the Si_3N_4 layer.

4.3 | Measurement Methods

The thickness of the samples is determined by the analysis of cross-section images obtained using a scanning electron microscope (Zeiss Merlin FE-SEM). Our samples exhibit a pyramidal surface texture. Consequently, the reported thickness is defined as the average between the base thickness and the base + top of the pyramid thickness.

Current–voltage (J–V) measurements are performed using two different setups. The first setup is used to measure all devices, whereas the second setup is exclusively employed for the measurement of the record solar cell. The first setup uses a Keithley 2611 voltage source and a Xenon lamp class ABA Oriel Sol2A sun simulator. The measurements are performed under a calibrated 1 Sun illumination. The second setup uses a two-lamp (Halogen and Xenon) class AAA WACOM Sun simulator. Before each measurement, the calibration of the AAA WACOM system is checked with three different certified cells with different spectral responses to minimize the spectral mismatch of the sources. Three-point weight maximum power point (MPP) measurements are performed using an in-house written LabVIEW code. For this setup, measurements are performed according to the standard testing procedure (1-sun, AM 1.5 Global, 25°C). Furthermore, a shadow mask is used to avoid back reflection of light because of the Au contact. The JV curves obtained from both setups are very similar. The V_{OC} and the FF are the same, whereas the J_{SC} is slightly smaller for the second setup ($\Delta J_{SC} \approx 0.5$ mA/cm^2).

External quantum efficiency (EQE) measurements are performed using an in-house built setup based on a Horiba micro HR grating monochromator and a Xe arc lamp source. The wavelength

spacing is set to 10 nm, the measurement range to 320–1050 nm and the voltage bias to 0 V.

Scanning electron microscopy (SEM) is performed in a Zeiss Gemini SEM 300 microscope operating in high vacuum mode. Secondary electron (SE) images are acquired with a Gemini II column in-lens SE detector at 3 keV electron beam energy with an injection current of 15 pA (as calibrated by a Faraday cup). Electron beam induced current (EBIC) measurements are performed on an Imina NANO platform compatible with the Zeiss electron microscope. Four miBots, each equipped with a 500 nm radius tungsten tip, are controlled individually via Precisio software. Piezoelectric motion ensured nanometer control over the electrical contacts to individual devices. EBIC measurements are performed at 3 keV acceleration voltage and 400 pA injected current. Experiments are performed by applying an external bias ranging from –1 V to +1 V (with 0.1 V or 0.2 V steps) through a Point Electronic amplifier controlled by a Digital Imaging scanning system. For all reported measurements, the hole-rich Zn_3P_2 layer is connected to the negative pole and the electron-rich InP substrate is connected to the positive pole. The current induced at the heterointerface is therefore measured as positive.

The outdoors PV evaluation was implemented in Hellenic Mediterranean University (HMU) campus and specifically at the open-air lab of HMU. More details on the facility and the equipment can be found in previous studies [47, 48]. Zn_3P_2 solar cells were placed on customized printed circuit boards (PCBs). These PCBs were mounted on aluminum holders with tunable height and angle in relation to the Sun allowing achieving the optimal conditions for highest energy output for the whole year (namely, south orientation and 29° degrees inclination due to the geographic location of the lab). Optical inspection took place in regular periodic intervals to associate any potential physical change before and after measurements, as well as during harsh environmental periods. We used a specific measurement protocol for all outdoor diurnal measurements. Specifically, each measurement was initiated at sunrise and ended at sunset with a one-minute step interval. For the J–V electrical characterization, the SMU-Infinity PV ISOS Testing Laboratory was used. A concurrent, continuous weather monitoring was implemented based on a meteorological station from Campbell Scientific CR1000× model with Pyranometer sensor Kipp & Zonen CMP3 for solar irradiance measurements. Type K thermocouples were placed on the back side of Zn_3P_2 solar cells for temperature measurements. The electrical characterization includes reverse J–V scans, with voltage sweeps from open circuit to short circuit conditions using a voltage step of 1 mV.

Three-dimensional optical simulations are performed using Ansys Lumerical software to obtain the optical generation rate profiles within the absorbing regions of the device. The generation profile is then integrated into the electrical simulations which are performed using Nextnano GmbH software [49, 50]. The general method for the simulations is explained in more details in our recent simulation study [23]. In our work, surface texturing is addressed by the incorporation of pyramids onto the thin film. The dimensions of the model (i.e. film thickness, pyramid height and angle) are directly extracted from SEM measurements of the experimental samples' cross-sections. Specific materials parameters used in this study for the electrical simulation are provided in the Table S1.

4.4 | Samples Description

Two sets of samples are prepared for this study. The first set consists of samples grown at 290°C with a V/II flux ratio of 0.36. The growth duration is varied from 4 to 8.5 h. Solar cell devices and EBIC devices are fabricated for all samples of this set (and for all pattern dimensions). The second set consists of samples grown varying the temperature from 280°C to 300°C. Because of the temperature-dependent growth rate, the duration is adjusted to target similar thickness for all samples. Solar cell devices are fabricated for all samples of this set (and for all pattern dimensions). Finally, some devices of the second set are annealed at 300°C for 30 min. One of them, grown from a 45/400 pattern (45 nm hole size/400 nm pitch), gives the record efficiency.

Acknowledgments

This work was supported by the Swiss State Secretariat for Education, Research and Innovation (SERI) under contract number 22.00018 and by Horizon Europe through the Pathfinder project SOLARUP (project number: 101046297). The authors also acknowledge the Center of MicroNanoTechnology (CMI) and the Interdisciplinary Center for Electron Microscopy (CIME) of EPFL for their technical support. VP gratefully acknowledges funding from SNSF Spark, grant CRSK-2-221120 and EPFL internal funding (VPA support to research n° 5178). EPFL authors also acknowledge the technical advice provided by IMINA Technologies SA.

Open access publishing facilitated by Ecole polytechnique federale de Lausanne, as part of the Wiley - Ecole polytechnique federale de Lausanne agreement via the Consortium Of Swiss Academic Libraries.

Conflicts of Interest

The authors declare no conflicts of interest.

Data Availability Statement

Raw data are available on Zenodo at doi:10.5281/zenodo.19335001.

References

1. J. Misiewicz, "Inter-Band Transitions in Zn3P2," *Journal of Physics: Condensed Matter* 2 (1990): 2053–2072.

2. T. Suda and K. Kakishita, "Epitaxial Growth of Zinc Phosphide," *Journal of Applied Physics* 71, no. 6 (1992): 3039–3041, https://doi.org/10.1063/1.350989.

3. E. Z. Stutz, S. P. Ramanandan, M. Fl'or, et al., "Stoichiometry Modulates the Optoelectronic Functionality of Zinc Phosphide ($Zn_{3-x}P_{2+x}$)," *Faraday Discussions* 239 (2022): 202–218, https://doi.org/10.1039/d2fd00055e.

4. M. Bhushan and A. Catalano, "Polycrystalline Zn3P2 Schottky Barrier Solar Cells," *Applied Physics Letters* 38, no. 1 (1981): 39–41, https://doi.org/10.1063/1.92124.

5. R. Paul, N. Humblot, S. E. Steinvall, et al., "Van der Waals Epitaxy of Earth-Abundant Zn3P2 on Graphene for Photovoltaics," *Crystal Growth & Design* 20, no. 6 (2020): 3816–3825, https://doi.org/10.1021/acs.cgd.0c00125.

6. J. P. Bosco, G. M. Kimball, N. S. Lewis, and H. A. Atwater, "Pseudomorphic Growth and Strain Relaxation of α-Zn3P2 on GaAs(001) by Molecular Beam Epitaxy," *Journal of Crystal Growth* 363 (2013): 205–210, https://doi.org/10.1016/j.jcrysgro.2012.10.054.

7. A. Tiede, R. Lemerle, T. Hagger, et al., "Long-Term Protection of Crystalline Zinc Phosphide (Zn3P2) Under Atmospheric Conditions," *APL Materials* 14, no. 1 (2026): 011113, https://doi.org/10.1063/5.0309919.

8. S. Demers and A. van de Walle, "Intrinsic Defects and Dopability of Zinc Phosphide," *Physical Review B* 85, no. 19 (2012): 195208, https://doi.org/10.1103/PhysRevB.85.195208.

9. Z. Yuan, Y. Xiong, and G. Hautier, "First-Principles Study of Intrinsic and Hydrogen Point Defects in the Earth-Abundant Photovoltaic Absorber Zn3 P2," *Journal of Physical Chemistry A* 11 (2023): 20592–20600.

10. G. A. Lombardi, F. M. De Oliveira, M. D. Teodoro, and A. J. Chiquito, "Investigation of Trapping Levels in p-Type Zn3P2 Nanowires Using Transport and Optical Properties," *Applied Physics Letters* 112, no. 19 (2018), 193103, https://doi.org/10.1063/1.5026548.

11. R. Katsube, H. Hayashi, A. Nagaoka, K. Yoshino, Y. Nose, and Y. Shirai, "Growth and Characterization of Indium-Doped Zn3P2 Bulk Crystals," *Japanese Journal of Applied Physics* 55, no. 4 (2016): 041201, https://doi.org/10.7567/JJAP.55.041201.

12. A. Rajib, A. Hasan, and M. A. Rahman, "Enhancing the Efficiency of Earth-Abundant Zn3P2 SCs by In-Depth Numerical Analyses on Various Hole Transport Layers," *Solar Energy* 299 (2025): 113678, https://doi.org/10.1016/j.solener.2025.113678.

13. J. P. Bosco, D. O. Scanlon, G. W. Watson, N. S. Lewis, and H. A. Atwater, "Energy-Band Alignment of II-VI/Zn3P2 Heterojunctions from X-Ray Photoemission Spectroscopy," *Journal of Applied Physics* 113, no. 20 (2013): 203705, https://doi.org/10.1063/1.4807646.

14. T. Suda, "Zn3P2 ITO Solar Cell," *Japanese Journal of Applied Physics* 22 (1983): 656–658.

15. T. E. Fischer, "Photoelectric Emission and Work Function of InP," *Physical Review* 142, no. 2 (2 1966): 519–523, https://doi.org/10.1103/PhysRev.142.519.

16. T. Soma, J. Satoh, and H. Matsuo, "Thermal Expansion Coefficient of GaAs and InP," *Solid State Communications* 42, no. 12 (6 1982): 889–892, https://doi.org/10.1016/0038-1098(82)90233-2.

17. M. Zamani, E. Stutz, S. Escobar, et al., "The Path Towards 1 μm Monocrystalline Zn ₃P ₂ Films on InP: Substrate Preparation, Growth Conditions and Luminescence Properties," *Journal of Physics: Energy* 3, no. 3 (7 2021): 034011, https://doi.org/10.1088/2515-7655/abf723.

18. R. Paul, V. Conti, M. Zamani, et al., "Zn/P Ratio and Microstructure Defines Carrier Density and Electrical Transport Mechanism in Earth-Abundant Zn3-xP2+y Thin Films," *Solar Energy Materials and Solar Cells* 252 (2023): 112194, https://doi.org/10.1016/j.solmat.2023.112194.

19. R. Paul, S. W. Tabernig, J. Re n'e Sapera, et al., "Carrier Generation and Collection in Zn3P2/InP Heterojunction Solar Cells," *Solar Energy Materials and Solar Cells* 256 (2023): 112349, https://doi.org/10.1016/j.solmat.2023.112349.

20. E. Z. Stutz, M. Zamani, D. A. Damry, et al., "Showcasing the Optical Properties of Monocrystalline Zinc Phosphide Thin Films as an Earth-Abundant Photovoltaic Absorber," *Materials Advances* 3, no. 2 (2022): 1295–1303, https://doi.org/10.1039/d1ma00922b.

21. S. Escobar Steinvall, E. Z. Stutz, R. Paul, et al., "Towards Defect-Free Thin Films of the Earth-Abundant Absorber Zinc Phosphide by Nanopatterning," *Nanoscale Advances* 3, no. 2 (2021): 326–332, https://doi.org/10.1039/d0na00841a.

22. R. Lemerle, H. Rabelo, T. Hagger, et al., "Nanopatterning Optimization of Zinc Phosphide: Hole Mobility up to 560 cm2/Vs with Selective Area Epitaxy," *Journal of Materials Chemistry C* 14 (2026): 8950–8959, https://doi.org/10.1039/D5TC03582A.

23. M. Micali, R. Lemerle, A. Tiede, A. Fontcuberta i Morral, and E. Alarc'on-Llad'o, "Optimizing Carrier Collection in Solar Cells Through Nanoscale Junction Design," *Energy Advances* 5 (2026): 427–433, https://doi.org/10.1039/D5YA00251F.

24. J. Yoo, J. Cho, K. Han, and J. Yi, "RIE Surface Texturing for Optimum Light Trapping in Multicrystalline Silicon Solar Cells," *Journal of the Korean Physical Society* 60, no. 12 (2012): 2071–2074, https://doi.org/10.3938/jkps.60.2071.

25. O. V. Feklisova, V. I. Orlov, and E. B. Yakimov, "EBIC and LBIC Investigations of Dislocation Trails in Si," *Physica Status Solidi C* 12 (2015): 1081–1084.

26. V. Piazza, M. Vettori, A. A. Ahmed, et al., "Nanoscale Investigation of a Radial p–n Junction in Self-Catalyzed GaAs Nanowires Grown on Si (111)," *Nanoscale* 10, no. 43 (2018): 20207–20217, https://doi.org/10.1039/C8NR03827A.

27. M. T. Borgstrom, M. H. Magnusson, F. Dimroth, et al., "Towards Nanowire Tandem Junction Solar Cells on Silicon," *IEEE Journal of Photovoltaics* 8, no. 3 (2018): 733–740, https://doi.org/10.1109/JPHOTOV.2018.2816264.

28. H. Zhang, V. Piazza, V. Neplokh, et al., "Correlated Optical and Electrical Analyses of Inhomogeneous Core/Shell InGaN/GaN Nanowire Light Emitting Diodes," *Nanotechnology* 32, no. 10 (2021): 105202, https://doi.org/10.1088/1361-6528/abc70e.

29. P. Sutter, V. Piazza, P. Ghimire, A. Fontcuberta i Morral, and E. Sutter, "Single–Crystalline Lateral p-SnS/n–SnSe van der Waals Heterostructures by Vapor Transport Growth with In Situ Bi Doping," *Advanced Functional Materials* 36 (2025): e22666, https://doi.org/10.1002/adfm.202522666.

30. V. Piazza, L. Mancini, H.-L. Chen, S. Collin, and M. Tchernycheva, "Nanoscale Analyses Applied to Nanowire Devices," In *Semiconductors and Semimetals*, 98 (2018): 231–319.

31. M. Tchernycheva, G. Jacopin, and V. Piazza, "Characterisation of Semiconductor Nanowires by Electron Beam Induced Microscopy and Cathodoluminescence," In *Fundamental Properties of Semiconductor Nanowires* (Springer, 2021), 251–288.

32. V. Piazza, S. Wirths, N. Bologna, et al., "Nanoscale Analysis of Electrical Junctions in InGaP Nanowires Grown by Template-Assisted Selective Epitaxy," *Applied Physics Letters* 114, no. 10 (2019): 103101, https://doi.org/10.1063/1.5085405.

33. P. Tchoulfian, F. Donatini, F. Levy, A. Dussaigne, P. Ferret, and J. Pernot, "Direct Imaging of p–n Junction in Core–Shell GaN Wires," *Nano Letters* 14, no. 6 (2014): 3491–3498, https://doi.org/10.1021/nl5010493.

34. E. B. Yakimov, S. S. Borisov, and S. I. Zaitsev, "EBIC Measurements of Small Diffusion Length in Semiconductor Structures," *Semiconductors* 41, no. 4 (2007): 411–413, https://doi.org/10.1134/S1063782607040094.

35. H. J. Leamy, "Charge Collection Scanning Electron Microscopy," *Journal of Applied Physics* 53, no. 6 (1982): R51–R80, https://doi.org/10.1063/1.331667.

36. G. M. Kimball, A. M. Müller, N. S. Lewis, and H. A. Atwater, "Photoluminescence-Based Measurements of the Energy Gap and Diffusion Length of Zn3P2," *Applied Physics Letters* 95, no. 11 (2009), https://doi.org/10.1063/1.3225151.

37. C. Zhang, Z. Huang, W. Wang, H. Deng, and S. Cheng, "Theoretical Investigation of Defect Characteristics and Doping Effects in Zn3P2 for Photovoltaic Application," *Journal of Solid State Chemistry* 359 (7 2026): 125957, https://doi.org/10.1016/j.jssc.2026.125957.

38. H. Masui, *Introduction to the Light-Emitting Diode* (2022).

39. M. Tamura, T. Yodo, T. Saitoh, and J. Palmer, "Rearrangement of Misfit Dislocations in GaAs on Si by Post-Growth Annealing," *Journal of Crystal Growth* 150 (1995): 654–660, https://doi.org/10.1016/0022-0248(95)80290-S.

40. E. Yakimov, E. Yakimov, V. Orlov, and D. Gogova, "Some New Insights into the Impact of Annealing on Single Stacking Faults in 4H-SiC," *Superlattices and Microstructures* 120 (2018): 7–14, https://doi.org/10.1016/j.spmi.2018.05.014.

41. P. K. Song, H. Akao, M. Kamei, Y. Shigesato, and I. Yasui, "Preparation and Crystallization of Tin-Doped and Undoped Amorphous Indium

Oxide Films Deposited by Sputtering," *Japanese Journal of Applied Physics* 38, no. 9A (1999): 5224.

42. M. Gulen, G. Yildirim, S. Bal, A. Varilci, I. Belenli, and M. Oz, "Role of Annealing Temperature on Microstructural and Electro-Optical Properties of ITO Films Produced by Sputtering," *Journal of Materials Science: Materials in Electronics* 24, no. 2 (2013): 467–474, https://doi.org/10.1007/s10854-012-0768-8.

43. J. Haschke, R. Lemerle, B. Aïssa, et al., "Annealing of Silicon Heterojunction Solar Cells: Interplay of Solar Cell and Indium Tin Oxide Properties," *IEEE Journal of Photovoltaics* 9, no. 5 (2019): 1202–1207, https://doi.org/10.1109/JPHOTOV.2019.2924389.

44. S. Lange, A. Hahnel, C. Luderer, D. Adner, M. Bivour, and C. Hagendorf, "Microscopic Origins of Contact Deterioration During Annealing of Silicon Heterojunction Solar Cell Contacts," *IEEE Journal of Photovoltaics* 13, no. 6 (2023): 777–786, https://doi.org/10.1109/JPHOTOV.2023.3307822.

45. L. M. Shaker, A. A. Al-Amiery, M. M. Hanoon, W. K. Al-Azzawi, and A. A. H. Kadhum, "Examining the Influence of Thermal Effects on Solar Cells: A Comprehensive Review," *Sustainable Energy Research* 11, no. 1 (2024): 6, https://doi.org/10.1186/s40807-024-00100-8.

46. N. Y. Dzade, "Unravelling the Early Oxidation Mechanism of Zinc Phosphide (Zn3P2) Surfaces by Adsorbed Oxygen and Water: A First-Principles DFT-D3 Investigation," *Physical Chemistry Chemical Physics* 22, no. 3 (2020): 1444–1456, https://doi.org/10.1039/c9cp03902c.

47. S. Pescetelli, A. Agresti, G. Viskadouros, et al., "Integration of Two-Dimensional Materials-Based Perovskite Solar Panels into a Stand-Alone Solar Farm," *Nature Energy* 7, no. 7 (2022): 597–607, https://doi.org/10.1038/s41560-022-01035-4.

48. H. Nikbakht, P. Mariani, L. Vesce, et al., "Upscaling Perovskite Photovoltaics: From 156 cm2 Modules to 0.73 m2 Panels," *Advanced Science* 12, no. 22 (2025): 2416316, https://doi.org/10.1002/advs.202416316.

49. S. Birner, T. Zibold, T. Andlauer, et al., "Nextnano: General Purpose 3-D Simulations," *IEEE Transactions on Electron Devices* 54, no. 9 (2007): 2137–2142, https://doi.org/10.1109/TED.2007.902871.

50. A. Trellakis, T. Zibold, T. Andlauer, et al., "The 3D Nanometer Device Project Nextnano: Concepts, Methods, Results," *Journal of Computational Electronics* 5, no. 4 (2006): 285–289, https://doi.org/10.1007/s10825-006-0005-x.

Supporting Information

Additional supporting information can be found online in the Supporting Information section.

Supporting File: adfm77727-sup-0001-SuppMat.pdf.